AGU ADVANCING EARTH AND SPACE SCIENCES

Geophysical Research Letters

RESEARCH LETTER
10.1029/2025GL118053

Influences of Summer Northeastern Arctic Sea Ice on September Compound Heatwave and Drought Events in the South China

Jiani Zeng[1,2], Huixin Li[1,2,3], Huijun Wang[1,2,3], Yuan Yuan[1,2], and Mingkeng Duan[1,2,3]

[1]State Key Laboratory of Climate System Prediction and Risk Management/Key Laboratory of Meteorological Disaster, Ministry of Education/Collaborative Innovation Center on Forecast and Evaluation of Meteorological Disasters, Nanjing University of Information Science and Technology, Nanjing, China, [2]School of Atmospheric Sciences, Nanjing University of Information Science and Technology, Nanjing, China, [3]Southern Marine Science and Engineering Guangdong Laboratory, Zhuhai, China

Key Points:

- Interannual variations of compound heatwave and drought events (CHDEs) during September in South China (SC) are evaluated
- The meridional position of westerly jet accounts for the anomalous regional atmospheric circulations associated with the CHDEs in SC
- Positive Arctic Sea ice anomalies in summer may trigger a southeastward-propagating Rossby wave train that regulates CHDEs in SC

Supporting Information:

Supporting Information may be found in the online version of this article.

Correspondence to:

H. Li,
lihuixin@nuist.edu.cn

Citation:

Zeng, J., Li, H., Wang, H., Yuan, Y., & Duan, M. (2026). Influences of summer northeastern Arctic Sea Ice on September compound heatwave and drought events in the South China. *Geophysical Research Letters*, *53*, e2025GL118053. https://doi.org/10.1029/2025GL118053

Received 20 NOV 2025
Accepted 22 JAN 2026

Author Contributions:

Conceptualization: Jiani Zeng, Huixin Li, Huijun Wang
Data curation: Huixin Li
Formal analysis: Jiani Zeng
Investigation: Jiani Zeng, Huixin Li
Methodology: Huixin Li
Software: Jiani Zeng
Supervision: Huijun Wang, Mingkeng Duan
Writing – original draft: Jiani Zeng
Writing – review & editing: Huixin Li, Huijun Wang, Yuan Yuan, Mingkeng Duan

Abstract Compound heatwave and drought events (CHDEs) in South China (SC) have intensified in early autumn, yet their driving factor remains unclear. Based on reanalysis data and numerical experiments, this study investigates the potential influence of the summer northeastern Arctic Sea ice concentration (NEASIC) on the interannual variation of September CHDEs in the SC. Results demonstrate that positive NEASIC anomalies during summer trigger a quasi-barotropic Rossby wave train, originating over the Greenland Sea, arching across the North Atlantic and the Mediterranean–Caspian region, and extending into East Asia. This wave dynamically drives a northward-shifted and intensified East Asian subtropical jet and anomalous anticyclonic circulation over SC. The resulting subsidence induces moisture flux divergence, suppresses cloud cover, and enhances surface radiative forcing, explaining about 28.4% of the CHDEs variability per interquartile NEASIC increase. This mechanism enhances predictive frameworks for subtropical compound extremes, emphasizing the role of NEASIC in regional climate resilience strategies.

Plain Language Summary Through a combination of observations and climate model simulations, we identify a pan-Arctic influence on September compound heatwave and drought events (CHDEs) in South China (SC). Our analysis shows that increased summer sea ice concentration in the northeastern Arctic Sea initiates a chain reaction, generating large-scale atmospheric waves that propagate southeastward in the atmosphere. This teleconnection pattern produces two main effects over East Asia, including the East Asian jet stream shifts northward and persistent subsidence develop over the SC region. As a result, these atmospheric anomalies make the air drier by driving moisture flux divergence (winds that carry moisture away from the region), lead to clearer skies and stronger surface heating, creating favorable conditions for simultaneous heatwaves and droughts to occur. The CESM CAM5.3.1 model experiments confirm that the northeastern Arctic Sea ice variations may drive the variability in these compound events. Our results offer new insights into the factors influencing CHDEs over SC, highlighting the importance of incorporating summer Arctic–land interactions into regional climate prediction efforts.

1. Introduction

Compound heatwave and drought events (CHDEs) have intensified and occurred more frequently in a warming climate, posing escalating risks to natural and human systems (Mukherjee & Mishra, 2021; Ridder et al., 2022; Yu & Zhai, 2020). South China (SC), which mainly includes the Yangtze River Valley (YRV) in China, has become a global hotspot for CHDEs because of its increased susceptibility to climate change (Sun et al., 2023; L. Zhang et al., 2023). For instance, the extreme CHDE in 2022, the most severe event on record since 1961, resulted in 4 million hectares of cropland being damaged, over 38 million people affected by water supply disruptions, and over CNY 315 billion in economic losses (https://www.mem.gov.cn/). The region combines seasonally concentrated monsoonal rainfall, strong evaporative demand, intensive agriculture, dense population, and marked spatial hydroclimatic heterogeneity, making the region particularly vulnerable to concurrent hot and dry extremes (Yang et al., 2002; L. Wang et al., 2015; C. Wang et al., 2015; H. Zhang et al., 2019).

Although CHDEs occur throughout the growing season (April–October) (Zong et al., 2024), most existing research has concentrated on summer, leaving their seasonal diversity insufficiently characterized. However,

CHDEs beyond summer can be equally consequential. Early autumn CHDEs, such as the August–September 2009 event, have induced abrupt vegetation declines across the southern YRV (J. Li et al., 2021). Similarly, the spring 2019 CHDE in western SC caused more than 13,500 km^2 agricultural damage and severe water shortages for 7 million residents (Luo et al., 2022). Spring CHDEs can precondition soils and vegetation, amplifying summer drought risk and associated ecological stress (J. Li et al., 2022). Across seasons, CHDEs elevate wildfire risk by synchronizing high temperatures, moisture deficits, and fuel availability (Zong et al., 2024). These impacts make clear that CHDEs outside summer also deserve close attention to their underlying drivers.

Recent studies have emphasized how atmospheric patterns contribute to the heatwave and drought intensification in SC. Particularly, an anomalously northward Western Pacific Subtropical High (WPSH) and an eastward-extended South Asian High enhance subsidence and surface warming over central-eastern SC (D. Zhang et al., 2024; P. Zhang et al., 2024; S. Wang et al., 2021). Sea surface temperature (SST) anomalies further modulate regional moisture transport. El Niño–induced cyclonic anomalies suppress autumn rainfall by weakening the South China Sea monsoon (D. Zhang et al., 2024), whereas negative Indian Ocean SST anomalies strengthen the East Asian summer monsoon and exacerbate heatwave and drought conditions in SC (W. Wang et al., 2017). High-latitude forcing has also emerged as a contributing factor, with Barents Sea ice loss linked to enhanced summer CHDEs via Eurasian teleconnections (Z. Li et al., 2024). However, these mechanisms have been examined primarily for summer conditions, and the processes governing early autumn CHDEs, particularly their sensitivity to preseason Arctic Sea ice anomalies, remain largely unknown.

September marks a sharp dynamical transition in the East Asian climate system, and its circulation background differs fundamentally from that of summer. As the East Asian summer monsoon withdraws, monsoonal moisture transport collapses, and deep convection weakens. At the same time, the East Asian subtropical jet strengthens and shifts equatorward, forming the characteristic autumn flow pattern (Ding, 2007; Lu, 2004; B. Wang, 2006). This seasonal reconfiguration creates a thermodynamic and dynamical environment distinct from that of summer, indicating that mechanisms established for summer CHDEs cannot simply be applied to September conditions. Yet the processes shaping early autumn CHDEs, and whether they respond to preseason Arctic sea-ice variability, remain largely unknown.

This study addresses these gaps by examining CHDEs occurring in the SC during early autumn (September), a critical transition period from the retreat of summer monsoon to the onset of autumn rainfall. Specifically, we investigate two key questions: What regional atmospheric patterns drive the variability of early autumn CHDEs in the SC? Does preseason Arctic Sea ice variation contribute to these events through specific teleconnection pathways? By integrating observational analyses and model simulations, we identify a chain of mechanisms linking summer Arctic Sea ice variation to amplified SC CHDEs via Eurasian atmospheric wave trains. Our findings provide critical insights into seasonal climate prediction and highlight the urgency of incorporating Arctic linkages into climate risk assessments for the SC.

2. Data and Method

2.1. Data

This study uses the CN05.1 data sets, which provide gridded monthly precipitation and surface air temperature (SAT) data during 1961–2022. The data sets were developed using data from 2,416 stations across China (Wu & Gao, 2013). Additionally, this study uses the monthly atmospheric reanalysis data provided by ERA5, including geopotential height, meridional and zonal winds, vertical velocity, specific humidity, and net surface shortwave radiation. Besides, the monthly sea ice concentration data derived from the Met Office Hadley Centre Sea Ice and SST data set (HadISST.v1.1) are also used (Rayner et al., 2003). The period applied for the present analysis is from 1961 to 2022 and the data have been detrended before the analysis. All data sets have a spatial resolution of $1° \times 1°$.

2.2. Methods

The CHDE is defined based on the joint survival cumulative distribution method (AghaKouchak et al., 2014; H. Li et al., 2018). Monthly precipitation (X_1) and temperature (X_2) anomalies are considered simultaneously. We first calculate the marginal cumulative distribution functions $F_i(x_i) = P(X_i \leq x_i)$ for each variable, then derive the

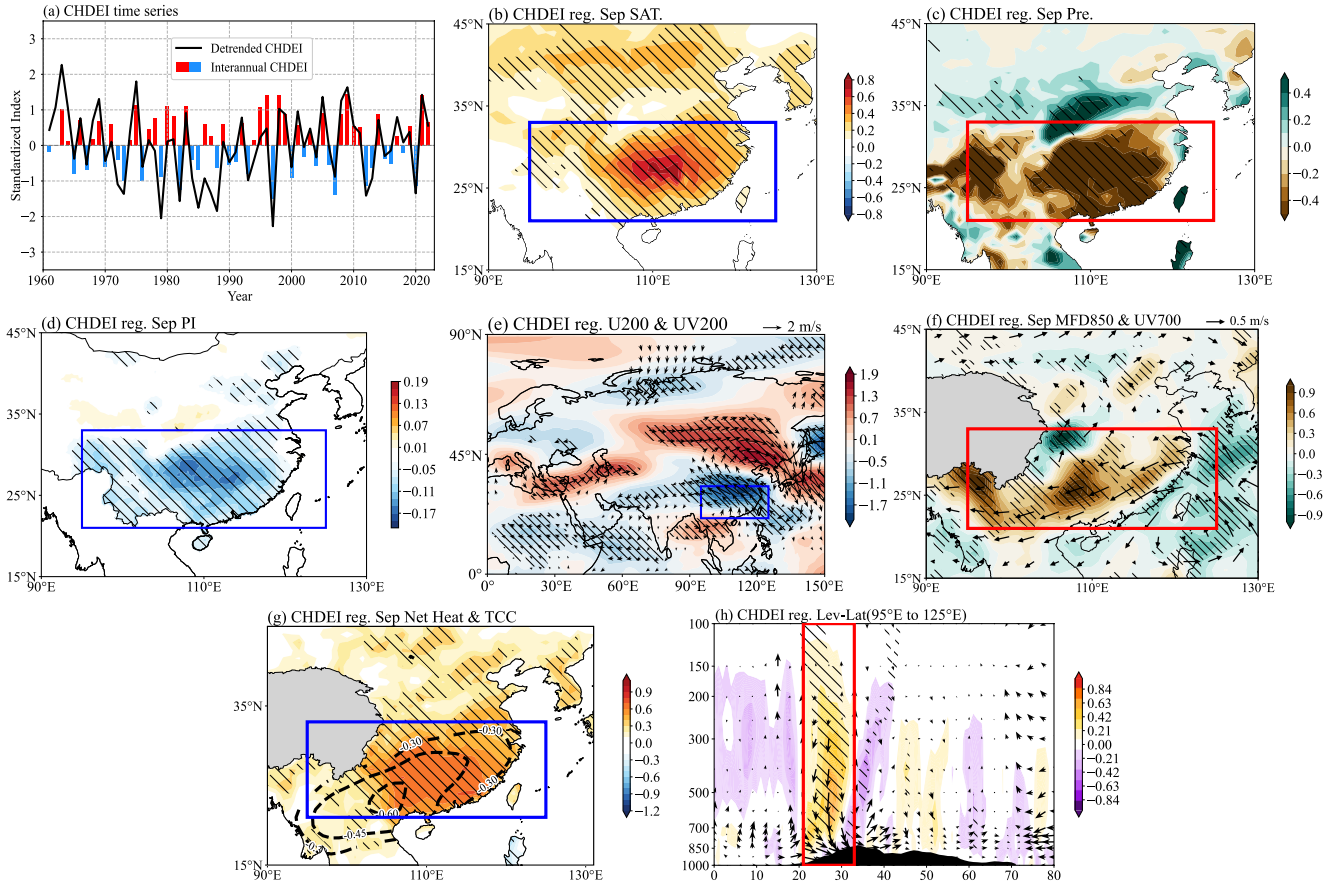

Figure 1. (a) The detrended and standardized temporal series of CHDEI over SC (black line; the regional mean PI multiplied by −1 in blue rectangle in b) in September and the corresponding interannual CHDEI component obtained from CEEMDAN (bars) during 1961–2022. Spatial distribution of the (b) SAT (unit: °C), (c) precipitation (unit: mm), and (d) probability-based index (PI; unit: 1) in September during 1961–2022 against the CHDEI. And the regression maps of September circulation against CHDEI: wind fields in (e) 200 hPa wind (vectors; unit: $m{\cdot}s^{-1}$) and 200 hPa zonal wind (shading; unit: $m{\cdot}s^{-1}$), (f) 700 hPa wind (vectors; unit: $m{\cdot}s^{-1}$) and 850 hPa moisture divergence flux (shading; unit: $kg{\cdot}m^{-2}\,s^{-1}$), and (g) regression maps of September total cloud cover (dotted line, unit: %) and net surface heat flux (shading, unit: $W{\cdot}m^{-2}$) and (h) vertical–horizontal cross section meridional wind (unit: $m{\cdot}s^{-1}$) and vertical velocity (ω, multiplied by 500; unit: $Pa{\cdot}s^{-1}$) averaged along 95°E–125°E. A positive net surface heat flux anomaly indicates a downward flux. The hatched regions indicate where the regression coefficient is significant at the 90% confidence level based on the *Student's t*-test.

survival functions $\overline{F_i} = 1 - F_i$, representing the probabilities of exceedance. The monthly CHDE index (CHDEI) is then computed via the *t*-copula method as a Probability Index (PI): $\mathrm{PI} = \hat{C}\left[\overline{F_1}(x_1), \overline{F_2}(x_2)\right] = P(X_1 > x_1, X_2 > x_2)$. Lower PI values indicate a higher likelihood of compound heatwave and drought events.

To extract the interannual variability of compound events, the Complete Ensemble Empirical Mode Decomposition with Adaptive Noise (CEEMDAN; Torres et al., 2011) is applied to the detrended standardized CHDEI during 1961–2022, the reconstructed interannual index is used in all subsequent analyses (Figure 1a). For the northeastern Arctic SIC, we isolate the interannual component by removing low-frequency variability with a 7-year high-pass Butterworth filter (Roberts & Roberts, 1978) applied to the detrended SIC time series. This filtering strategy ensures that the diagnosed relationships between CHDEI and Arctic SIC primarily reflect interannual co-variability.

2.3. Model Description and Experiment Design

The Community Atmosphere Model version 5.3.1 (CAM5.3.1) developed by NCAR is employed in this study. The model is configured at a horizontal resolution of 1.9° × 2.5°. Two experiments are conducted: a control simulation (CTRL) and a sensitivity experiment (EXP_NEA). In CTRL, the model is forced with monthly

climatological SIC and SST following the 1981–2010 mean. In EXP_NEA, SIC forcing is modified only over the northeastern Arctic (15°W–90°E, 65°–85°N). The imposed perturbation is constructed by regressing June–September SIC anomalies onto the standardized September CHDEI during 1961–2022. The regression is performed for each calendar month, and the resulting monthly perturbation fields are prescribed accordingly. The imposed SIC anomalies correspond to one standard deviation of observed variability, ensuring that the perturbation amplitude remains physically realistic. SST is kept identical to CTRL and is set to −1.8°C where SIC equals 1; elsewhere, SST remains unchanged. Thus, EXP_NEA differs from CTRL only in the prescribed SIC anomalies over the northeastern Arctic.

Both experiments are integrated for 40 years, with the first 20 years discarded as model spin-up and the remaining 20 years used for analysis. All prescribed boundary forcings are updated monthly.

3. Possible Physical Mechanism Underlying CHDEs in SC

3.1. Characteristics of CHDEs Variability and the Corresponding Atmospheric Circulation Anomalies

Spatial patterns of September CHDE variability over China during 1961–2022 exhibit pronounced regional contrasts (Figure S2 in Supporting Information S1). SC shows substantially larger standard deviations of the probability-based index (PI) than northern China, with values up to about 1.5 times higher, implying enhanced sensitivity to compound heatwave and drought conditions. Two particularly vulnerable areas are identified: the mid-Yangtze Valley (110°E, 25°N) and the eastern Tibetan Plateau (95°E, 25°N). Both regions exhibit exceptionally high variability, with standard deviation values exceeding 24, highlighting these areas as hotspots of September CHDE risk (Figure S2 in Supporting Information S1, contour).

To better characterize CHDE variability over the SC, we constructed a standardized CHDEI by averaging the PI values over 21°–33°N, 95°–125°E (shown as the rectangle in Figure 1b). We focused on the first intrinsic mode function (IMF1), which captures the dominant interannual fluctuations of CHDEI. IMF1 accounts for 65% of the total variance and represents the primary interannual variability, while higher-order IMFs mainly reflect lower-frequency fluctuations, which are not the focus of this study. Therefore, only IMF1 is retained for analysis. Because a lower PI indicates more severe CHDEs conditions, we define CHDEI = −PI so that higher values correspond to more severe CHDEs. After removing linear trends, the standardized and detrended CHDEI (Figure 1a, black line) shows a transition from predominantly below-average values before the late 1990s to enhanced positive anomalies after 2000, indicating an overall intensification of September CHDEs in SC, consistent with previous findings on the increasing concurrence of heatwaves and droughts in the Yangtze Basin (Jia et al., 2021; L. Wang et al., 2015; C. Wang et al., 2015).

Figure 1b–h illustrates the anomalous atmospheric circulation patterns associated with CHDEs over SC in September. CHDEs in this region are associated with distinct climatic conditions, including warmer temperatures (Figure 1b), reduced precipitation (Figure 1c), and lower PI values, indicative of severe compound extremes (Figure 1d). These conditions correspond closely to persistent significant anomalous anticyclones extending vertically from 700 to 200 hPa atmospheric levels over eastern Asia. Within the SC region, there is clear evidence of anomalous southeasterly winds at 200 hPa and anomalous divergence at 700 hPa (Figures 1e and 1f). Meanwhile, the axis of the East Asian Subtropical Westerly Jet (EASWJ) shifts toward the north and intensifies at approximately 45°N (Figure 1e). Furthermore, the northward displacement of the EASWJ axis contributes to a pronounced anomalous descending atmospheric motion on the right side of the jet exit region in the SC (Figure 1h) (Uccellini & Johnson, 1979). These synergistic upper-level dynamics (divergence aloft, jet reorganization) and lower-tropospheric forcing (subsidence, surface heating) form a coherent physical mechanism explaining intensified CHDEs under current climate conditions.

Moreover, during the occurrence of CHDEs, SC exhibits moisture flux divergence at 850 hPa (Figure 1f). Combined with enhanced atmospheric subsidence (Figure 1h), this reduction in moisture supply drives decreased precipitation (Figure 1c). Beyond precipitation deficits, temperature anomalies also play a crucial role in intensifying CHDEs. Anomalous subsidence (Figure 1h) and moisture flux divergence (Figure 1f) contribute to a reduction in total cloud cover (Figure 1g). Under these conditions, an increased amount of net radiation flux may penetrate the atmosphere and reach the surface (Figure 1g), thereby intensifying the heating effect on surface air (Figure 1b). Consequently, this combination of diminished precipitation and increased temperatures significantly enhances the likelihood of CHDEs occurrences in the SC (Figure 1d).

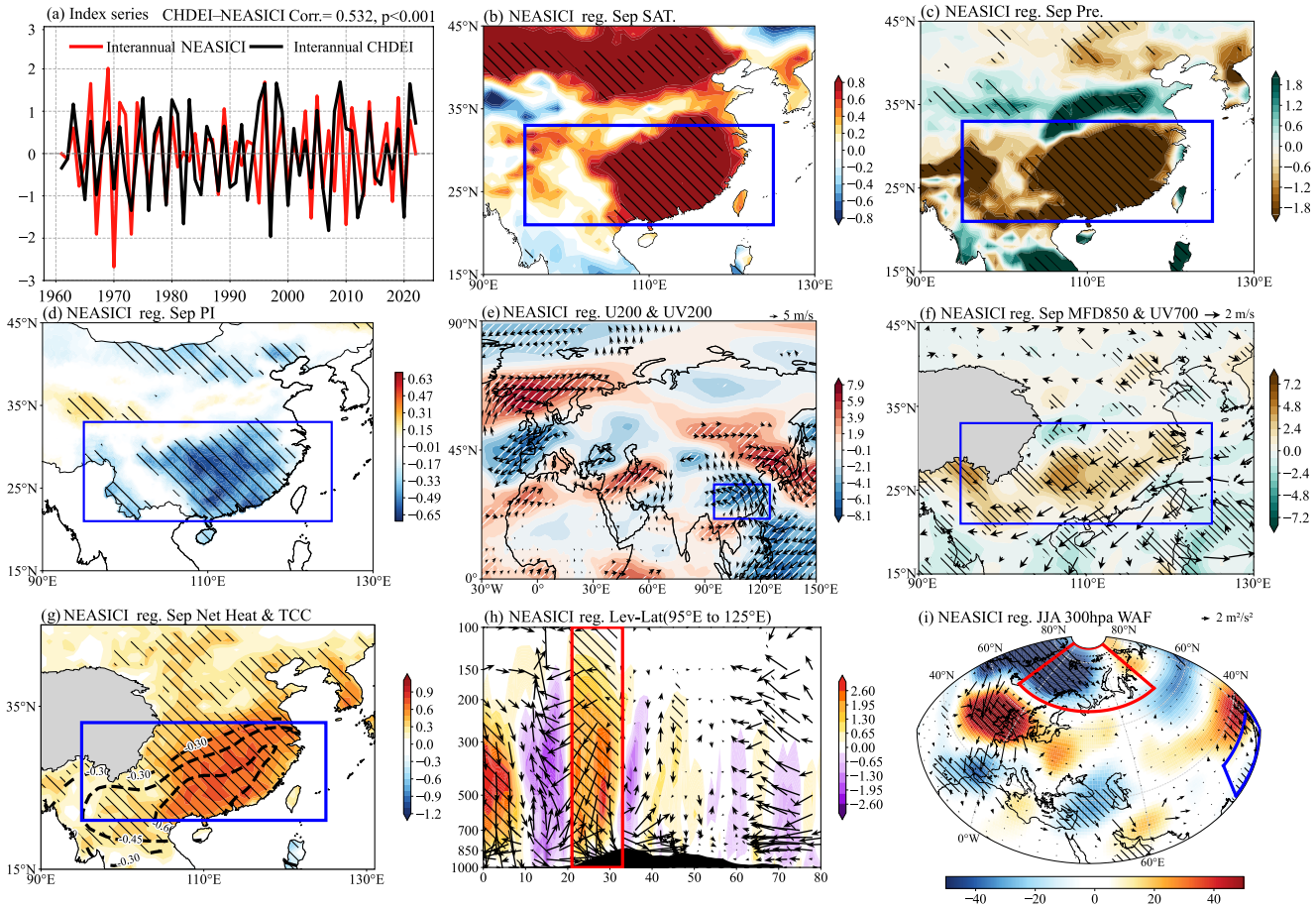

Figure 2. (a) Interannual time series of September SC CHDEI (black line) and interannual NEA sea ice concentration in summer during 1961–2022 (NEASICI, red line, the regional mean sea ice concentration in black rectangle in Figure S3 in Supporting Information S1). Spatial distribution of the (b) SAT (unit: °C), (c) precipitation (unit: mm), and (d) PI (unit: 1) in September during 1961–2022 against the NEASICI. Regressions of September (e) wind fields in 200 hPa wind (vectors; unit: $m{\cdot}s^{-1}$) and 200 hPa zonal wind (shading; unit: $m{\cdot}s^{-1}$); (f) 700 hPa wind (vectors; unit: $m{\cdot}s^{-1}$) and 850 hPa moisture flux divergence (shading; $kg{\cdot}m^{-2}\ s^{-1}$); (g) total cloud cover (dotted line; unit: %) and net surface heat flux (shading; unit: $W{\cdot}m^{-2}$); (h) vertical–horizontal cross section meridional wind ($m{\cdot}s^{-1}$) and vertical velocity (ω, multiplied by 200; $Pa{\cdot}s^{-1}$) averaged along 95°E–125°E; (i) 300 hPa geopotential height anomaly (shading; unit: m) and 300 hPa wave activity flux (vectors; unit: $m^2{\cdot}s^{-2}$) against NEASICI during 1961–2022. Positive net surface heat flux anomaly indicates downward flux. The dotted or shading regions indicate where the regression coefficient is significant at the 90% confidence level based on the *Student's t*-test.

3.2. Linking SC CHDEs to NEA Sea-Ice Anomalies

Arctic sea ice variability exerts a substantial influence on Eurasian climate (F. Li & Wang, 2012; X. Zhang et al., 2022), although the regional impacts vary considerably. Previous studies have primarily highlighted the influence of sea ice changes in the Barents-Kara Seas (Chen et al., 2019; He et al., 2018). However, our analysis highlights NEA Sea ice concentration (NEASIC) as an important driver of compound climate extremes in SC.

Specifically, increased summer NEASIC is closely associated with September CHDEs in the SC region. Figure 2a shows the correlation analysis of summer NEASIC against the September CHDEI. The results demonstrate a robust correlation between observed positive northern NEASIC anomalies during summer and CHDEs in the SC region. Furthermore, the summer NEASIC (defined as the average sea ice concentration in the key sea ice area: 15°W–90°E, 65°–85°N) alongside the September CHDEI in the SC is presented in Figure S3 in Supporting Information S1. Both indices exhibit distinct interannual variability. Upon detrending the NEASIC index (NEASICI) and CHDEI during 1961–2022, the correlation coefficient between the two is 0.532, which is statistically significant at the 99% confidence level, as determined by a *t*-test, indicating a robust linkage between enhanced NEA summer sea ice and intensified September CHDEs in SC.

To investigate the physical mechanisms behind this connection, we examine the atmospheric circulation anomalies in September regressed onto interannual NEASICI. Figures 2e and 2f illustrate that higher NEASICI is associated with a strengthened and northward-displaced EASWJ and a coherent anticyclonic anomaly extending from the lower to upper troposphere over East Asia, forming a quasi-barotropic high-pressure system (Figures 2e and 2f), that closely resembles the circulation pattern linked to positive CHDEI (Figure 1). These configuration favors clear-sky (Figure 2g), subsident conditions (Figure 2h) over SC during September.

Moisture and energy budgets further connect NEASICI to SC CHDEs. Under positive NEASICI phases, anomalous easterly flows weaken the transport of moist air from the Bay of Bengal and the Arabian Sea, leading to significant low-level moisture flux divergence over SC (Figure 2f) and suppressed precipitation. The drier, subsident environment is accompanied by reduced cloud cover and enhanced downward net surface radiation (Figure 2g), which amplify near-surface warming (Figure 2b) and precipitation shortage (Figure 2c). Together, these circulation, moisture, and radiative anomalies provide a dynamically consistent pathway through which increased NEA summer sea ice is linked to more frequent and intense September CHDEs in SC (Figure 2d).

Figure 2i further illustrates the upper-tropospheric Rossby wave response associated with summer NEASICI. Regressed 300-hPa geopotential height anomalies and wave activity flux (WAF) vectors show a pronounced southward-propagating wave train originating from the Greenland Sea, propagating into the Mediterranean, then eastward along the Mediterranean–Caspian Sea corridor, and extending downstream into East Asia. The wave pattern links enhanced NEA sea-ice conditions to the reorganization of the East Asian jet and subtropical circulation, thereby establishing a dynamical bridge between Arctic forcing and September climate anomalies over SC.

We further quantify how NEA summer sea-ice anomalies affect September climate conditions and CHDEs in SC. A one-interquartile (IQR) increase in summer NEASICI is associated with a warming of approximately 0.18°C in September SAT over SC ($r = 0.40$, $p < 0.01$), explaining about 15.9% of its interannual variance. At the same time, September precipitation decreases by around 0.48 mm month^{-1} ($r = -0.70$, $p < 0.01$), accounting for about 48.3% of the interannual variance. Consistently, regression analyses indicate that a one-IQR increase in summer NEASICI enhances the September CHDEI over SC by about 0.66 ($r = 0.53$, $p < 0.01$), explaining 28.4% of its interannual variance. Although NEASICI alone explains only part of the observed variability, its associated thermodynamic and dynamical impacts—such as Rossby wave propagation and jet-stream modulation—help establish a large-scale background state that favors the co-occurrence of heatwaves and droughts. These results support the interpretation of NEA summer sea-ice anomalies as an effective precursor modulating CHDEs in SC.

Additionally, positive NEASIC anomalies (NEASICA) are accompanied by negative sea surface temperature (Figure 3a) and reduced turbulent heat flux anomalies (Figure 3b), indicating suppressed ocean–atmosphere heat exchange. The resulting surface cooling appears as negative 2-m air temperature anomalies (Figure 3c) and extends upward, which favors anomalous subsidence (Figure 3d), which in turn induces an upper-level low over the NEA sector (Figure 2i), forming the upstream center of action for the subsequent Rossby wave response.

3.3. Numerical Experiments

Observational analysis suggests that the Rossby wave train triggered by summer NEASICA provides an atmospheric connection that intensifies CHDEs in the SC. To further validate this linkage, we conducted two numerical modeling experiments. By comparing atmospheric responses in sensitivity experiments (with altered NEA Sea ice conditions) to control runs, we assessed how variations in NEASIC influence CHDE formation over the SC.

Figure 4 shows that NEASICA triggers a Rossby wave train originating from the NEA, extending across the North Atlantic toward the Mediterranean–Caspian region, and subsequently propagating eastward to eastern Asia. This simulated teleconnection pattern closely resembles the observed WAF and circulation response associated with positive NEASICI. This teleconnection pattern drives three key dynamical responses over SC: northward displacement of the EASWJ (Figure 4c), lower-tropospheric divergence (700 hPa, Figure 4d) coupled with subsidence (Figure 4f), and moisture flux divergence (Figure 4d). Collectively, these conditions result in regional precipitation reduction (Figure 4b) and elevated surface temperatures (Figure 4a), consistent with increased

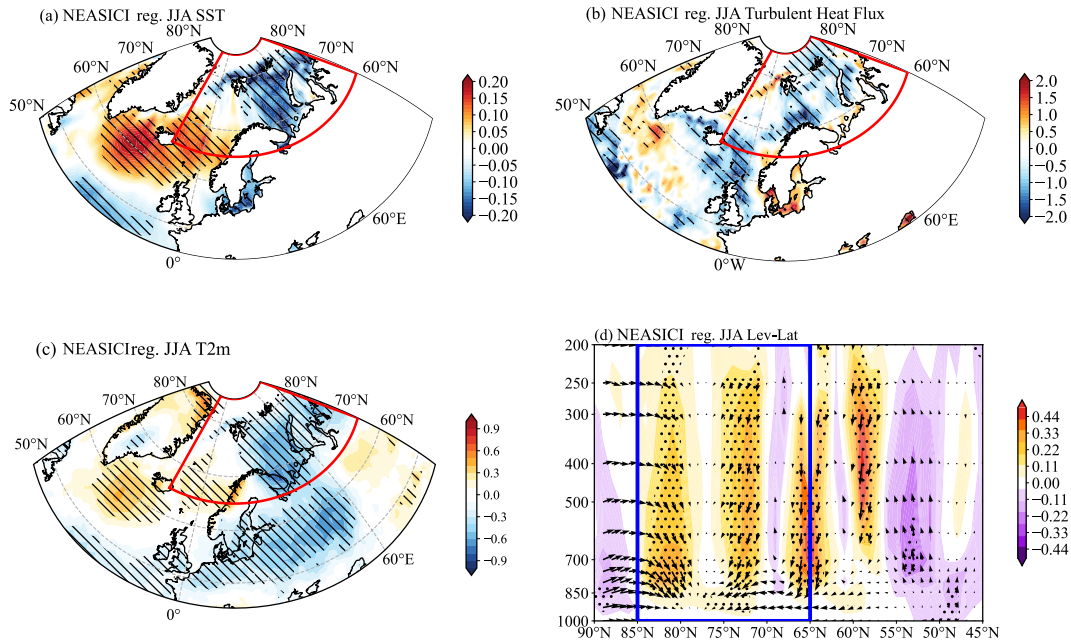

Figure 3. Regression maps of (a) June, July, and August (JJA) sea surface temperature against NEASICI (unit:°C), (b) JJA turbulent heat flux (unit: 10^{-6} W·m^{-2}), and (c) JJA 2 m temperature (unit:°C), (d) JJA vertical–horizontal cross section averaged along 30°E–60°E with regard to summer NEASICI from 1961 to 2022 (vectors; include horizontal wind, unit: m·s^{-1}, and vertical velocity ω, multiplied by 1,000, unit: Pa·s^{-1}) (Regression coefficients significant at the 90% confidence level are plotted with black dots or shading based on *t*-test.).

surface net heat flux (Figure 4e). Thus, the NEASICA-triggered teleconnection orchestrates a dynamic pathway that culminates in the September CHDE over SC.

4. Conclusion and Discussion

This study reveals that a robust dynamical linkage between NEASICA and September CHDEs in SC. Based on CHDEI and circulation diagnostics for 1961–2022, we show that intensified September CHDEs in SC are systematically associated with a northward-displaced and strengthened EASWJ, an anomalous anticyclonic circulation, enhanced subsidence, low-level moisture flux divergence, reduced cloud cover, and increased downward net surface radiation. This circulation–moisture–radiation configuration provides a dynamically coherent framework that favors concurrent heat and drought in early autumn.

We further demonstrate that increased summer NEASIC serves as an effective large-scale precursor for these circulation anomalies and associated CHDEs. After removing decadal variability, positive NEASICI is linked to a pronounced upper-tropospheric Rossby wave train originating over the Greenland Sea sector, arching across the North Atlantic and the Mediterranean–Caspian region, and extending into East Asia. This quasi-stationary wave pattern reorganizes the East Asian jet and subtropical high, changing the anticyclonic, subsident, and moisture-divergent conditions over SC that promote September CHDEs. Statistically, a one-interquartile increase in summer NEASICI explains about 28.4% of the interannual variance of September CHDEI, together with substantial fractions of the variance in surface temperature and precipitation, underscoring the importance of NEA Sea ice variability as a key modulator of SC's early autumn compound extremes.

Idealized sensitivity experiments with CAM5 corroborate this Arctic–Eurasian teleconnection. Perturbed NEASIC forcing in the NEA induces a Eurasian wave-train–like response, a northward-shifted and strengthened East Asian jet, and an anomalous anticyclone over SC, leading to reduced precipitation, enhanced surface heating, and intensified CHDEs. The close agreement between model responses and observational regressions lends dynamical support to the proposed mechanism linking NEA Sea ice to September CHDEs in SC.

Nevertheless, Arctic forcing alone does not fully determine CHDE variability, other climate factors must also be considered. Large-scale phenomena such as the North Atlantic Oscillation (López-Moreno et al., 2011), El Niño–

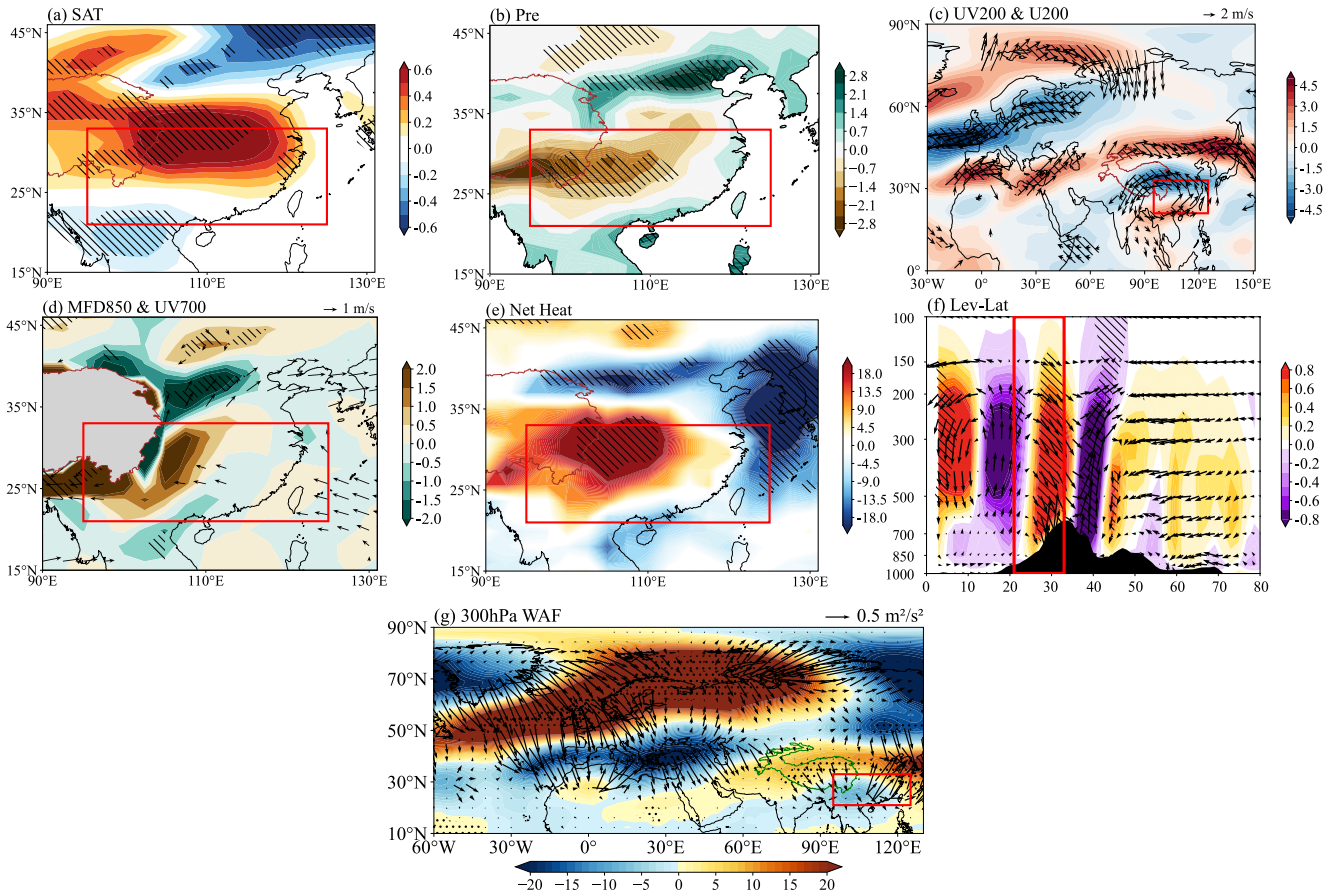

Figure 4. Numerical simulations of EXP_NEA in modulating CHDEs in the SC. The composite differences of (a) SAT (unit: °C), (b) precipitation (PRE, unit: mm), (c) 200 hPa zonal wind (shading; unit: m·s^{-1}) and wind field (vectors; unit: m·s^{-1}), (d) 700 hPa wind (vectors; unit: m·s^{-1}) and 850 hPa moisture flux divergence (shading; unit: kg·m^{-2} s^{-1}), and (e) net surface heat flux (unit: W·m^{-2}). (f) Vertical–horizontal cross section averaged along 95°–125°E (units: m·s^{-1} and Pa·s^{-1}), (g) 300 hPa geopotential height anomaly (shading; unit: m) and 300 hPa wave activity flux (vectors; unit: m^2·s^{-2}). All results are based on the numerical simulation in September between the sensitivity run and control experiments of CAM5. The black dotted or shading regions indicate the anomalies significant at 90% confidence level based on the *Student's t*-test.

Southern Oscillation (Hao et al., 2018), and Atlantic Multidecadal Oscillation (H. Li et al., 2020), can alter the East Asian summer monsoon and broader atmospheric circulation, thereby affecting CHDE frequency and intensity (Pan et al., 2024). Regionally, the position and intensity of the WPSH, EASWJ, and summer monsoons shape temperature and precipitation anomalies that modulate CHDEs, particularly in the SC region (Z. Li et al., 2024). Additionally, land–atmosphere interactions—such as Tibetan Plateau snow cover—can influence large-scale circulation and further regulate CHDEs variability (Yao et al., 2024). Future work should employ high-resolution Earth System Models, together with process-based diagnostics, to quantify the relative contributions and possible nonlinear interactions among Arctic Sea ice, tropical SSTs, and land-surface processes to CHDEs across seasons. Such efforts are essential for improving subseasonal-to-seasonal predictions and risk-informed adaptation strategies for CHDEs in SC.

Conflict of Interest

The authors declare no conflicts of interest relevant to this study.

Data Availability Statement

The ERA5 monthly averaged data on single levels (Hersbach et al., 2023a, 2023b) and pressure levels (Hersbach et al., 2023a, 2023b) were obtained from the Copernicus Climate Change Service. The HadISST1.1 sea surface temperature and sea ice concentration data set (Rayner et al., 2003) was sourced from the Met Office Hadley

Centre. The CAM5.3.1 climate model used for sensitivity experiments is provided by NCAR (Neale et al., 2012). The standardized CHDEI for South China during 1961–2022 is available via Zeng and Li (2025).

Acknowledgments
This research was supported by the National Natural Science Foundation of China (Grant 42575029).

References

AghaKouchak, A., Cheng, L., Mazdiyasni, O., & Farahmand, A. (2014). Global warming and changes in risk of concurrent climate extremes: Insights from the 2014 California drought. *Geophysical Research Letters*, *41*(24), 8847–8852. https://doi.org/10.1002/2014GL062308

Chen, S., Wu, R., & Chen, W. (2019). Enhanced impact of Arctic sea ice change during boreal autumn on the following spring Arctic oscillation since the mid-1990s. *Climate Dynamics*, *53*(9–10), 5607–5621. https://doi.org/10.1007/s00382-019-04886-y

Ding, Y. (2007). The variability of the Asian summer monsoon. *Journal of the Meteorological Society of Japan. Series II*, *85B*(85B), 21–54. https://doi.org/10.2151/jmsj.85B.21

Hao, Z., Hao, F., Singh, V. P., & Zhang, X. (2018). Quantifying the relationship between compound dry and hot events and El Niño–southern Oscillation (ENSO) at the global scale. *Journal of Hydrology*, *567*, 332–338. https://doi.org/10.1016/j.jhydrol.2018.10.022

He, S., Gao, Y., Furevik, T., Wang, H., & Li, F. (2018). Teleconnection between sea ice in the Barents Sea in June and the Silk Road, Pacific–Japan and East Asian rainfall patterns in August. *Advances in Atmospheric Sciences*, *35*(1), 52–64. https://doi.org/10.1007/s00376-017-7029-y

Hersbach, H., Bell, B., Berrisford, P., Biavati, G., Horányi, A., Muñoz Sabater, J., et al. (2023a). ERA5 monthly averaged data on single levels from 1940 to present. *Copernicus Climate Change Service (C3S) Climate Data Store (CDS)*. https://doi.org/10.24381/cds.f17050d7

Hersbach, H., Bell, B., Berrisford, P., Biavati, G., Horányi, A., Muñoz Sabater, J., et al. (2023b). ERA5 monthly averaged data on pressure levels from 1940 to present. *Copernicus Climate Change Service (C3S) Climate Data Store (CDS)*. https://doi.org/10.24381/cds.6860a573

Jia, X., Gu, Q., Qian, Q., & Wu, R. (2021). Wet-to-dry climate shift of the Sichuan Basin during 1961–2010. *Climate Dynamics*, *57*(3–4), 671–685. https://doi.org/10.1007/s00382-021-05734-8

Li, F., & Wang, H. (2012). Autumn sea ice cover, winter Northern Hemisphere annular mode, and winter precipitation in Eurasia. *Journal of Climate*, *26*(11), 3968–3981. https://doi.org/10.1175/JCLI-D-12-00380.1

Li, H., Chen, H., Wang, H., Sun, J., & Ma, J. (2018). Can Barents Sea ice decline in spring enhance summer hot drought events over northeastern China? *Journal of Climate*, *31*(12), 4705–4725. https://doi.org/10.1175/JCLI-D-17-0429.1

Li, H., He, S., Gao, Y., Chen, H., & Wang, H. (2020). North Atlantic modulation of interdecadal variations in hot drought events over northeastern China. *Journal of Climate*, *33*(10), 4315–4332. https://doi.org/10.1175/JCLI-D-19-0440.1

Li, J., Bevacqua, E., Chen, C., Wang, Z., Chen, X., Myneni, R. B., et al. (2022). Regional asymmetry in the response of global vegetation growth to springtime compound climate events. *Communications Earth & Environment*, *3*(1), 123. https://doi.org/10.1016/j.ecolind.2023.111253

Li, J., Wang, Z., Wu, X., Zscheischler, J., Guo, S., & Chen, X. (2021). A standardized index for assessing sub-monthly compound dry and hot conditions with application in China. *Hydrology and Earth System Sciences*, *25*(3), 1587–1601. https://doi.org/10.5194/hess-25-1587-2021

Li, Z., Ren, H. L., Lu, M., & Zhou, F. (2024). Interannual variations of westward extension area of western Pacific subtropical high and its relationship with precipitation in East Asia. *Atmospheric Research*, *298*, 107148. https://doi.org/10.1016/j.atmosres.2023.107148

López-Moreno, J. I., Vicente-Serrano, S. M., Morán-Tejeda, E., Lorenzo-Lacruz, J., Kenawy, A., & Beniston, M. (2011). Effects of the North Atlantic Oscillation (NAO) on combined temperature and precipitation winter modes in the Mediterranean mountains: Observed relationships and projections for the 21st century. *Global and Planetary Change*, *77*(1–2), 62–76. https://doi.org/10.1016/j.gloplacha.2011.03.003

Lu, R. Y. (2004). Associations among the components of the East Asian summer monsoon system in the meridional direction. *Journal of the Meteorological Society of Japan*, *82*(1), 155–165. https://doi.org/10.2151/jmsj.82.155

Luo, F., Wang, S., He, Y., Wang, Y., & Wang, H. (2022). Anthropogenic warming has increased the 2020 extreme hot and dry conditions over Southwest China. *Bulletin of the American Meteorological Society*, *103*(3), S124–S129. https://doi.org/10.1175/BAMS-D-21-0208.1

Mukherjee, S., & Mishra, A. K. (2021). Increase in compound drought and heatwaves in a warming world. *Geophysical Research Letters*, *48*(1), e2020GL090617. https://doi.org/10.1029/2020GL090617

Neale, R. B., Chen, C.-C., Gettelman, A., Lauritzen, P. H., Park, S., Williamson, D. L., & Taylor, M. A. (2012). *Description of the NCAR Community atmosphere model (CAM 5.0) (NCAR Technical note nos. NCAR/TN-486+STR)*. National Center for Atmospheric Research. Retrieved from https://www.cesm.ucar.edu/models/cesm1.2/cam/

Pan, X., Wang, W., Shao, Q., Wei, J., Li, H., Zhang, F., et al. (2024). Compound drought and heat waves variation and association with SST modes across China. *Science of the Total Environment*, *907*, 167934. https://doi.org/10.1016/j.scitotenv.2023.167934

Rayner, N. A. A., Parker, D. E., Horton, E. B., Folland, C. K., Alexander, L. V., Rowell, D. P., et al. (2003). Global analyses of sea surface temperature, sea ice, and night marine air temperature since the late nineteenth century. *Journal of Geophysical Research*, *108*(D14). https://doi.org/10.1029/2002JD002670

Ridder, N. N., Ukkola, A. M., Pitman, A. J., & Perkins-Kirkpatrick, S. E. (2022). Increased occurrence of high impact compound events under climate change. *npj Climate and Atmospheric Science*, *5*(1), 3. https://doi.org/10.1038/s41612-021-00224-4

Roberts, J., & Roberts, T. D. (1978). Use of the Butterworth low-pass filter for oceanographic data. *Journal of Geophysical Research*, *83*(C11), 5510–5514. https://doi.org/10.1029/JC083iC11p05510

Sun, B., Xue, R., Li, W., Zhou, S., Li, H., Zhou, B., & Wang, H. (2023). How does Mei-Yu precipitation respond to climate change? *National Science Review*, *10*(12), nwad246. https://doi.org/10.1093/nsr/nwad246

Torres, M. E., Colominas, M. A., Schlotthauer, G., & Flandrin, P. (2011). A complete ensemble empirical mode decomposition with adaptive noise. In *2011 IEEE international conference on acoustics, speech and signal processing (ICASSP)* (pp. 4144–4147). IEEE. https://doi.org/10.1109/ICASSP.2011.5947265

Uccellini, L. W., & Johnson, D. R. (1979). The coupling of upper and lower tropospheric jet streaks and implications for the development of severe convective storms. *Monthly Weather Review*, *107*(6), 682–703.

Wang, B. (2006). *The Asian monsoon*. Springer.

Wang, C., Zou, J., Mai, B., Chen, H., Tang, L., & Duan, H. (2015). Temporal-spatial characteristics and its variation trend of meteorological drought in recent 50 years, South China. *Acta Ecologica Sinica*, *35*(3), 595–602. https://doi.org/10.5846/stxb201304120691

Wang, L., Chen, W., Zhou, W., & Huang, G. (2015). Drought in Southwest China: A review. *Atmospheric and Oceanic Science Letters*, *8*(6), 339–344. https://doi.org/10.3878/AOSL20150043

Wang, S., Huang, J., & Yuan, X. (2021). Attribution of 2019 extreme spring–early summer hot drought over Yunnan in southwestern China. *Bulletin of the American Meteorological Society*, *102*(1), S91–S96. https://doi.org/10.1175/BAMS-D-20-0121.1

Wang, W., Xu, J., Cai, X., & Sun, C. (2017). Analysis of atmospheric circulation characteristics and mechanism of heat wave and drought in summer of 2013 over the middle and lower reaches of Yangtze River Basin. *Plateau Meteorology*, *36*(6), 1595–1607. https://doi.org/10.7522/j.issn.1000-0534.2016.00129

Wu, J., & Gao, X. J. (2013). A gridded daily observation dataset over China region and comparison with the other datasets. *Chinese Journal of Geophysics*, *56*(4), 1102–1111. https://doi.org/10.6038/cjg20130406

Yang, J., Ding, Y., Chen, R., & Liu, L. (2002). The interdecadal fluctuation of dry and wet climate boundaries in China in recent 50 years. *Acta Geographica Sinica*, *57*(6), 655–661. https://doi.org/10.1007/BF02837476

Yao, H., Zhao, L., Shen, X., Ding, Y., Wang, J., & Xiao, Z. (2024). Synergistic impacts of wintertime regional snow anomalies in the Northern Hemisphere on the summer rainfall pattern in China. *Environmental Research Letters*, *19*(1), 014064. https://doi.org/10.1088/1748-9326/ad178d

Yu, R., & Zhai, P. (2020). More frequent and widespread persistent compound drought and heat event observed in China. *Scientific Reports*, *10*(1), 14576. https://doi.org/10.1038/s41598-020-71312-3

Zeng, J., & Li, H. (2025). Standardized compound heatwave and drought events index (CHDEI) for South China, 1961–2022 (1.0.0) [Dataset]. *Zenodo*. https://doi.org/10.5281/zenodo.15585659

Zhang, D., Huang, Y., Zhou, B., Wang, H., & Sun, B. (2024). Who is the major player for 2022 China extreme heat wave? Western Pacific Subtropical high or South Asian high? *Weather and Climate Extremes*, *43*, 100640. https://doi.org/10.1016/j.wace.2024.100640

Zhang, H., Wu, C., & Hu, B. X. (2019). Recent intensification of short-term concurrent hot and dry extremes over the Pearl River basin, China. *International Journal of Climatology*, *39*(13), 4924–4937. https://doi.org/10.1002/joc.6116

Zhang, L., Yu, X., Zhou, T., Zhang, W., Hu, S., & Clark, R. (2023). Understanding and attribution of extreme heat and drought events in 2022: Current situation and future challenges. *Advances in Atmospheric Sciences*, *40*(11), 1941–1951. https://doi.org/10.1007/s00376-023-3171-x

Zhang, P., Wang, B., Wu, Z., Jin, R., & Cao, C. (2024). Intensified gradient La Niña and extra-tropical thermal patterns drive the 2022 East and South Asian "Seesaw" extremes. *npj Climate and Atmospheric Science*, *7*(1), 47. https://doi.org/10.1038/s41612-024-00597-2

Zhang, X., Wu, B., & Ding, S. (2022). Influence of spring Arctic sea ice melt on Eurasian surface air temperature. *Climate Dynamics*, *59*(11), 3305–3316. https://doi.org/10.1007/s00382-022-06267-4

Zong, X., Liu, Y., & Yin, Y. (2024). Identifying the dominant compound events and their impacts on vegetation growth in China. *Weather and Climate Extremes*, *45*, 100715. https://doi.org/10.1016/j.wace.2024.100715